JOURNAL OF AIRCRAFT
Vol. 34, No. 1, January–February 1997

Effect of Geometry on the Unsteady Type-IV Shock Interaction

Charles A. Lind*
U.S. Naval Academy, Annapolis, Maryland 21402

This work describes the effect of cowl geometry on the unsteady behavior of a type-IV shock interaction. The numerical procedure used for the thin-layer approximation to the compressible Navier–Stokes calculations is a second-order central difference approximation for the diffusion terms and a total variation diminishing type scheme for the inviscid terms. The calculations show that the peak surface pressure, the impingement location of the supersonic jet, and the time required for the development of the interaction are functions of both the impinging shock location and the cowl geometry. In addition, it is shown that the peak pressure loads associated with the type-IV shock interaction can be reduced by changing the geometric shape of the cowl.

Nomenclature

A, B = grid clustering parameters
a = speed of sound
D, H = grid clustering parameters
l = length scale
M = Mach number
p = pressure
t = time
u, v = x, y component of velocity
x, y = physical coordinates
β = shock angle
$\Delta( )$ = change in ( )
θ = angular measurement
ξ, η = transformed coordinates

Subscripts
c = circular cylinder
j = jet
j, k = grid indices
r = residual
s = shock
t = total
v = viscous
w = wall
∞ = freestream

Superscript
n = Y-coordinate exponent

Introduction

ONE of the most challenging problems associated with the design of hypersonic vehicles is the accurate prediction of the interaction between the oblique shocks that form on the primary vehicle surfaces and the curved shocks that form on the protruding, secondary surfaces of the vehicle, as shown in Fig. 1, or of the hypersonic waverider, described in detail by Bowcutt.[1]

Presented as Paper 95-3157 at the AIAA/SAE/ASME/ASEE 31st Joint Propulsion Conference and Exhibit, San Diego, CA, July 10–12, 1995; received Aug. 6, 1995; revision received Sept. 21, 1996; accepted for publication Nov. 1, 1996.

*Visiting Professor, Department of Aerospace Engineering; currently Office of Naval Research Postdoctoral Fellow, Laboratory for Computational Physics, Naval Research Laboratory, Washington, DC 20375-5344. E-mail: lind@lcp.nrl.navy.mil. Senior Member AIAA.

Since these transatmospheric vehicles will require aerodynamic control surfaces, thrusters, or even engine integration to successfully complete their missions, an environment will exist for the formation of detached, curved shocks. The interaction of the primary oblique shocks with the curved shocks can result in a very complex flowfield with extremely high pressure and heat transfer loads in a localized region. Experimental as well as computational results have shown that these pressure loads and heating rates can be up to 30 times larger than those of the noninterfering case.[2–8] The associated large-temperature gradients and attendant thermal stresses resulting from such an interaction may severely limit the life of these structural components or perhaps the usefulness of the vehicle.

The type-IV shock interaction is one of six types of shock interactions first categorized by Edney.[2] The six different shock interaction patterns are shown in Fig. 2 and the type IV is described in more detail in Fig. 3.

It has been experimentally shown that for the type-IV shock interaction, the peak pressure, heat transfer rates, and pressure distributions are sensitive to upstream thermodynamic flow conditions, shock strength, and Mach number.[2,3,9] In addition, recent experimental[3,10] and computational[4–8] work indicates that the type-IV interaction is unsteady. In particular, for the geometries studied, interaction frequencies on the order of 1–30 kHz were found.

Since it is desirable to find new ways to minimize the effects of the heat and pressure loads on the engine cowl (because of the shock on shock interactions) as well as to decrease the effect of the shock reflections within the engine, resulting in

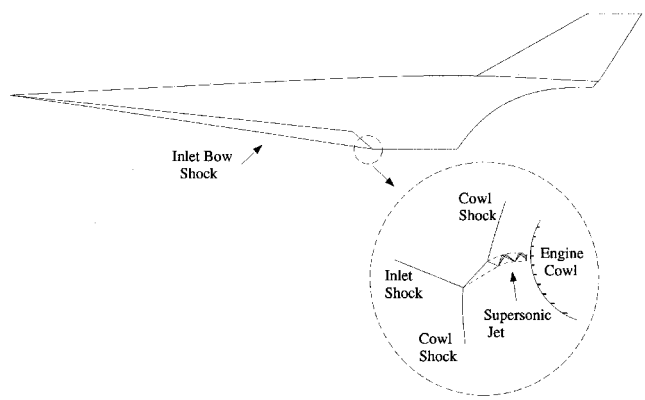

Fig. 1 Generic hypersonic vehicle showing the type-IV shock interaction.

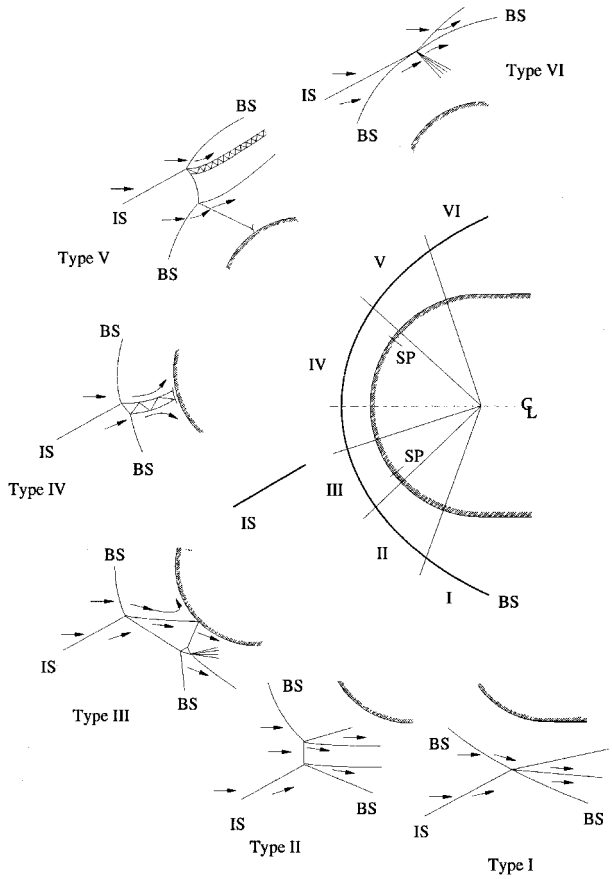

Fig. 2 Six types of shock interaction patterns: SP, sonic point; IS, impinging shock; and BS, bow shock.

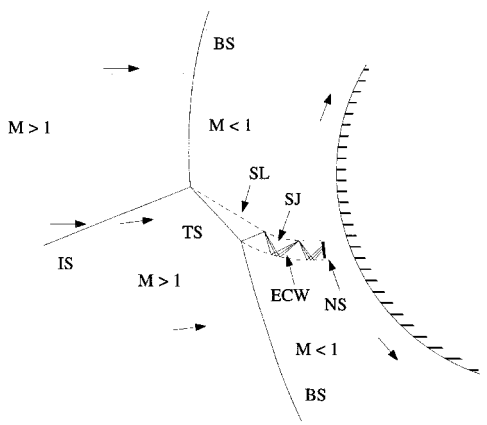

Fig. 3 Type-IV shock interaction: BS, bow shock; ECW, expansion/compression waves; IS, impinging shock; NS, normal shock; SL, shear layer; SJ, supersonic jet; and TS, transmitted shock.

shock-/boundary-layer interactions, a geometric change in the engine cowl is studied.

This work considers, for the first time, the effect of impinging shock location on the type-IV interaction for a variety of cowl leading-edge geometries. In addition to parametric studies, the time-accurate variation of the peak surface pressure is presented, as is the time evolution of the interaction. Detailed flowfield analysis is also performed from which conclusions can be drawn about the effect of engine cowl geometry.

Numerical Algorithm

The approach to high-resolution upwind schemes is incorporated in the prevention of numerical oscillations, as opposed to classical methods where oscillations are damped out after they have occurred. It is for this reason that a high resolution scheme, in particular the total variation diminishing (TVD) algorithm, was selected for this work.

The original TIMETVD code, which forms the basis for the present work, was derived from the ARC2D code developed at NASA Ames Research Center. The ARC2D code solves the thin-layer approximation to the Navier–Stokes equations in generalized curvilinear coordinates. The inviscid portion of ARC2D with the TVD algorithm was also modified at NASA Ames Research Center. The numerical algorithm is an implicit approximate factorization finite difference scheme (ADI). The TVD scheme used in the present code, which was developed by Yee and Harten,[11] gives second-order accuracy in space and time. Roe's averaging is used to describe the inviscid components of the flux. The entropy fix of Harten, with Yee's second-order corrections is implemented,[11] and the explicit viscous terms are centrally differenced.

The original ARC2D code has been validated by Pulliam,[12] the original TIMETVD code by Montagne and Yee,[13] and the present version of the TIMETVD code by Lind.[7]

Initial and Boundary Conditions

To initiate the time-accurate solution of the shock interaction flowfield, a blunt body solution is first calculated for each geometry. A straight oblique shock (of a given strength defined by β) is then introduced into the flowfield such that it intersects the initial bow shock formed on the blunt body solution at an angle given by θ_s, as shown in Fig. 4.

At the body surface a zero-pressure gradient and constant wall temperature is assumed.

The outflow boundary, which is supersonic for all calculations, is extrapolated from the adjacent grid point. For the blunt body calculations, freestream values are used for all points on the inflow boundary. For the shock interaction cases, freestream conditions are assigned to the points on the inflow boundary above the shock impingement point and values given by the Rankine–Hugoniot equation, for the given freestream Mach number and shock strength, are assigned to the remaining inflow points.

Grid Generation

Each grid in this study resulted from a two-step grid-generation process: an algebraic grid smoothed by an elliptic solver. The algebraic grid algorithm generated the body, outside boundary, and clustered grid points circumferentially in regions of interest. Specifically, the points on the outside boundary were clustered near the impinging shock location and points on the solid boundary were clustered near the impingement point of the supersonic jet. An elliptic solver was utilized to ensure smoothness of the grid, orthogonality of the grid lines at the solid surface, and grid clustering at the solid boundary.

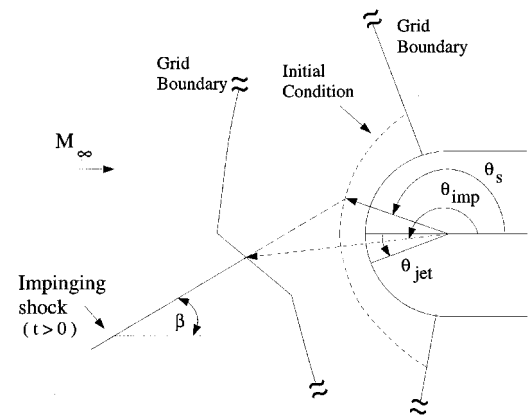

Fig. 4 Nomenclature used in the discussion.

Algebraic Grid Generation

The solid body, for each geometry, was modeled by scaling the y coordinate of a circular body of a given radius. In particular, for any given x coordinate, the y coordinate of the new cowl geometry is given by

$$y(x) = y_c(x)^n \tag{1}$$

where y_c is the y coordinate of the circle and n is a number in the range $1.0 \leq n \leq 1.2$. This is shown schematically in Fig. 5. The geometries used in this work are shown schematically in Fig. 6. In this figure, $y = y_c{**}1.00$ corresponds to the circular cylinder and is shown as a reference.

The freestream boundary was generated using the shock correlations of Billig.[14] The upper and lower portions of the outside boundary were calculated independently so as to conform to the geometry of the type-IV interaction. The upper and lower portions of the outer boundary were connected by a straight line.

Clustering in the circumferential direction was performed separately on the solid and outside boundary and was accomplished by using the following stretching function from Hoffmann[15]:

$$x = \xi \qquad y = D\left\{1 + \frac{\sinh[B(\eta - A)]}{\sinh(BA)}\right\} \tag{2a}$$

where A is given by

$$A = \frac{1}{2B}\,\ell n\,\frac{1 + (e^{B} - 1)(D/H)}{1 + (e^{-B} - 1)(D/H)} \tag{2b}$$

In Eqs. (2a) and (2b), B is the grid clustering parameter and controls the amount of clustering, H is the total length of the direction being considered, D is the y coordinate where clustering is desired and ξ and η are the coordinates in the computational space.

Elliptic Grid Generation

To ensure orthogonality at the solid surface and to smooth the grid, the elliptic grid generation algorithm developed by Sorenson[16] is used. In addition to grid orthogonality, the algorithm also allowed the user to specify the spacing between the solid body and the grid point immediately above it, Δs_{body}. A typical grid used in this study is shown in Fig. 7. All grids used in this study had a constant Δs_{body} of 3×10^{-6} m.

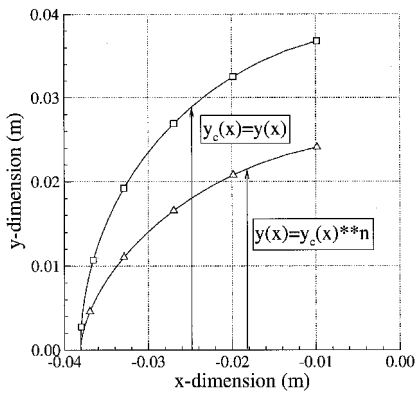

Fig. 5 Description of surface boundary.

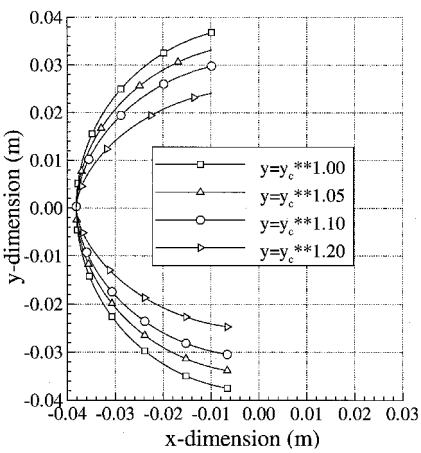

Fig. 6 Four different geometries used in this study.

Results

Initial Blunt Body Solutions

The initial condition for each of the runs (for each geometry) was a converged blunt body solution (i.e., no impinging shock). The blunt body calculation was considered converged

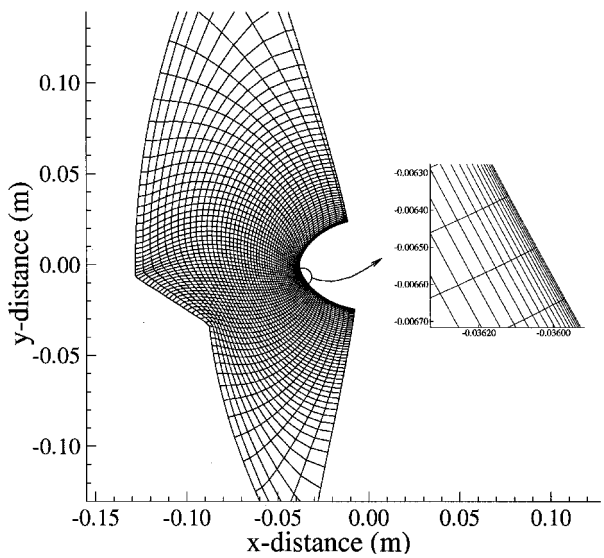

Fig. 7 Typical 179 × 160 elliptic grid (n = 1.2 and every third point in the ξ and η direction is shown). Inset highlights body region (every grid point is shown).

Table 1 Summary of shock interference studies[a]

n = 1.0		n = 1.05		n = 1.1		n = 1.2	
Shock equation	θ_s	Shock equation	θ_s	Shock equation	θ_s	Shock equation	θ_s
$y = mx + 0.03151$	168.2	$y = mx + 0.02365$	171.1	$y = mx + 0.02019$	173.7	$y = mx + 0.01663$	176.0
$y = mx + 0.02959$	170.0	$y = mx + 0.02135$	173.8	$y = mx + 0.01902$	175.1	$y = mx + 0.01601$	176.9
$y = mx + 0.02656$	172.9	$y = mx + 0.01902$	176.5	$y = mx + 0.01723$	177.3	$y = mx + 0.01476$	178.6
$y = mx + 0.02365$	175.7	$y = mx + 0.01601$	179.9	$y = mx + 0.01601$	178.8	$y = mx + 0.01283$	181.0
$y = mx + 0.02019$	179.1	$y = mx + 0.01476$	181.3	$y = mx + 0.01413$	181.1	$y = mx + 0.01081$	183.7
$y = mx + 0.01601$	182.9	$y = mx + 0.01283$	183.5	$y = mx + 0.01081$	185.0	$y = mx + 0.00941$	185.5
$y = mx + 0.01283$	185.9	$y = mx + 0.01149$	185.1	$y = mx + 0.00941$	186.7	$y = mx + 0.00796$	187.3

[a] The equations describe the impinging shock, $m = 0.331613$ (19 deg) and θ_s is the location on the bow shock where the oblique shock impinges.

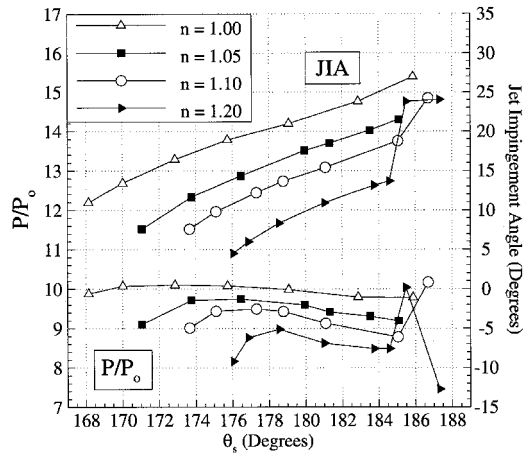

Fig. 8 Effect of impinging shock location θ_s on the peak pressure and JIA for each geometry.

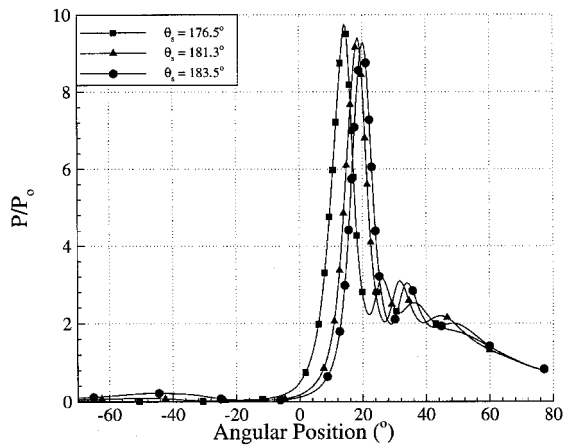

Fig. 9 Comparison of surface pressure for n = 1.05 and various SIAs.

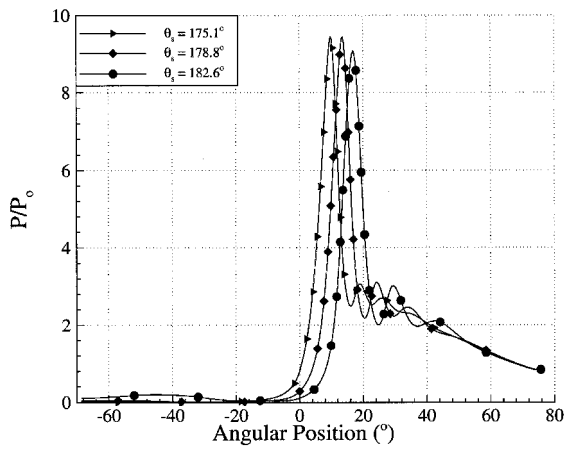

Fig. 10 Comparison of surface pressure for n = 1.1 and various SIAs.

when the L_2 norm of the density residual dropped below 10^{-10}. The L_2 norm of the density residual is defined as

$$\|\rho_r\|_2 = \sqrt{\sum_{j=1}^{j\max}\sum_{k=1}^{k\max}\rho_{rj,k}^2}\Big/\sqrt{j_{\max}k_{\max}}\Delta t \qquad (3)$$

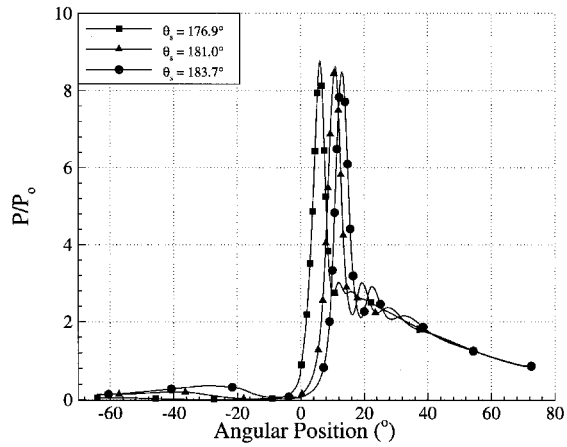

Fig. 11 Comparison of surface pressure for n = 1.2 and various SIAs.

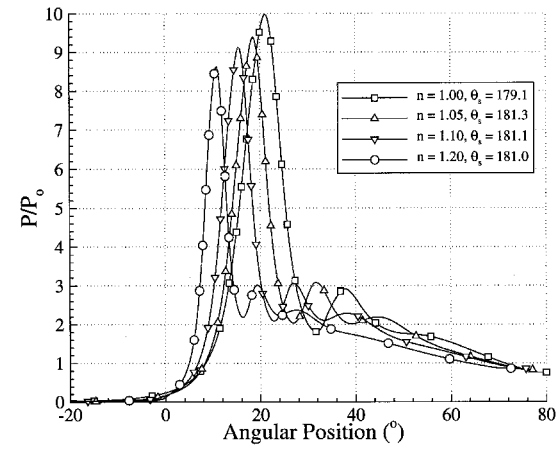

Fig. 12 Comparison of surface pressure for various geometries with $\theta_s \approx$ 181 deg.

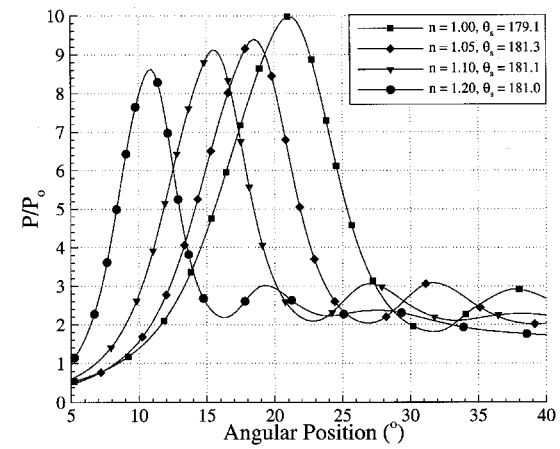

Fig. 13 Close view of surface pressure for various geometries with $\theta_s \approx$ 181 deg.

where $\rho_{rj,k}$, the residual of the density, is defined as the difference in the value of density between two time integration steps

$$\rho_{rj,k} = \rho_{j,k}^{n+1} - \rho_{j,k}^{n} \qquad (4)$$

In this work only the pressure calculations are performed. To accurately predict the heat transfer in this work, it is estimated that $\Delta\eta$ would have to be at least 10^{-9} m, as discussed by Lind.[7] Since grid spacing of this order would drastically

increase the computational effort required, and since this work is directed more toward the unsteady phenomena, which pressure measurements can accurately analyze, heat transfer results were not calculated.

Parametric Studies

The flow conditions used in this work are based on those used by Holden et al.[17] for run 24. Specifically, $M_\infty = 8.144$, $Re/\text{m} = 1.243 \times 10^7$, and $T_{\text{wall}} = 954$ K. All calculations were performed with an impinging shock angle of 19 deg. Three different geometries were studied ($n = 1.05$, 1.1, and 1.2) and were compared with the results for $n = 1.0$[8]. The cases studied are summarized in Table 1. A constant time step of 2×10^{-7} s was used for all calculations.

The overall trends for the four different geometries, shown in Fig. 8, are similar and are to be expected. First, as the impinging shock location moves downward (from $\theta_s < 180$ deg to $\theta_s > 180$ deg), the supersonic jet location also moves downward. Also, the peak surface pressure reaches a maximum, for each geometry, which is to be expected since the other inter-

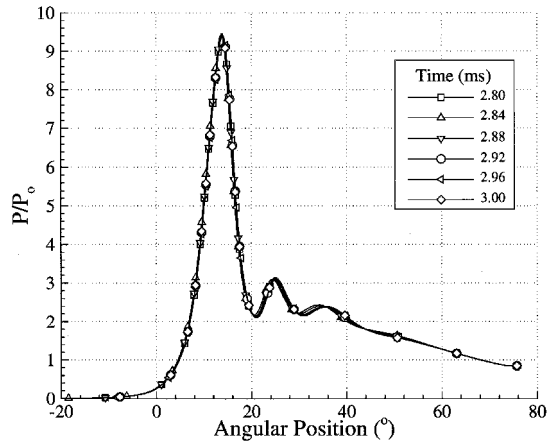

Fig. 14 Time history of the surface pressure over one cycle for the $n = 1.1$ and $\theta_s = 178.8$-deg calculation.

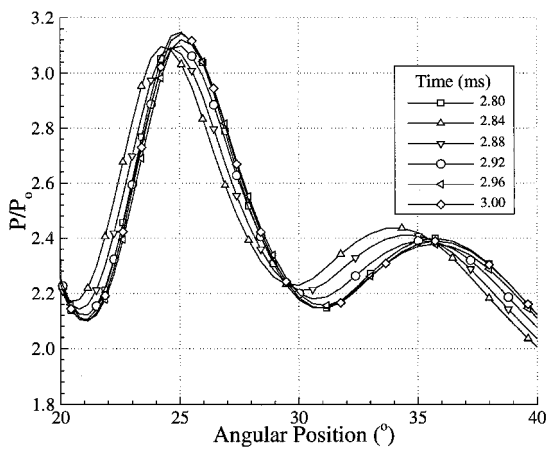

Fig. 15 Close view of time history of the surface pressure over one cycle for the $n = 1.1$ and $\theta_s = 178.8$-deg calculation.

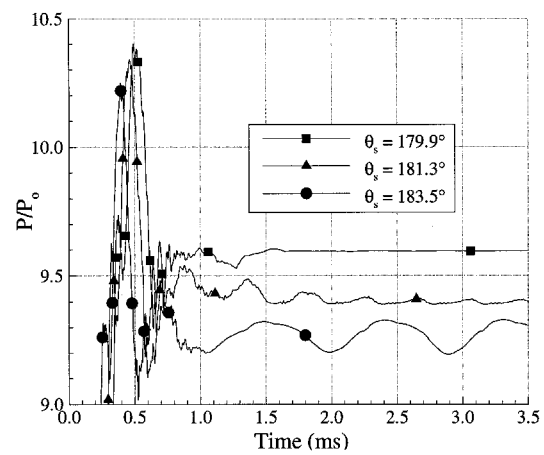

Fig. 16 Time variation of peak pressure for the geometry $y = y_c^{1.05}$ with $179.9 \geq \theta_s \leq 183.5$ deg.

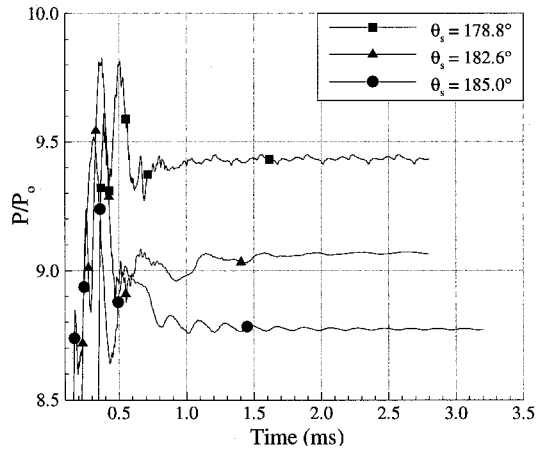

Fig. 17 Time variation of peak pressure for the geometry $y = y_c^{1.1}$ with $178.8 \geq \theta_s \leq 185.0$ deg.

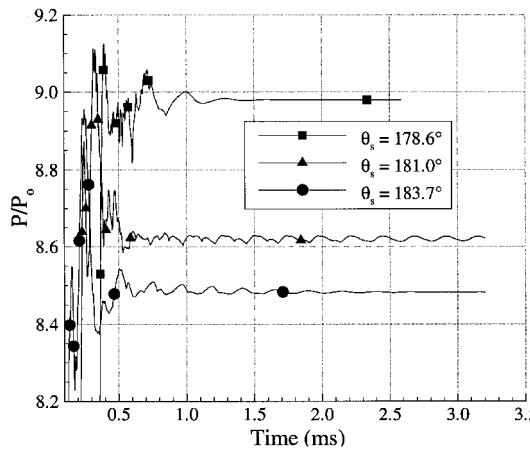

Fig. 18 Time variation of peak pressure for the geometry $y = y_c^{1.2}$ with $178.6 \geq \theta_s \leq 183.7$ deg.

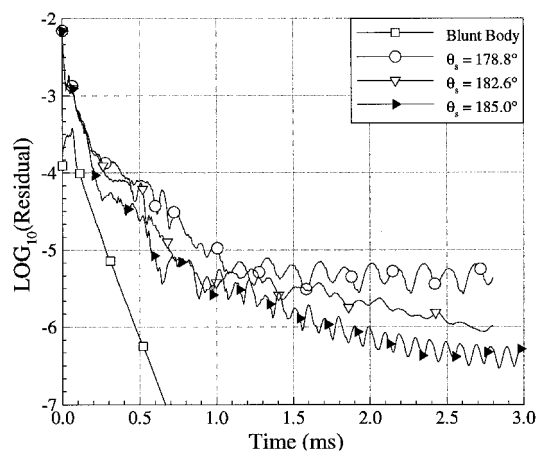

Fig. 19 L_2 norm of the density residual for the geometry $y = y_c^{1.1}$ for various θ_s.

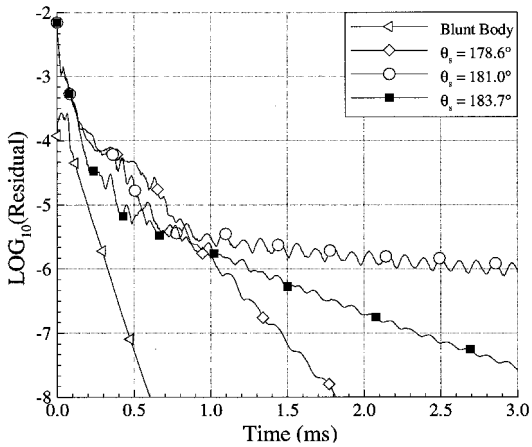

Fig. 20 L_2 **norm of the density residual for the geometry** $y = y_c^{1.2}$ **for various** θ_s.

actions have a lower peak surface pressure than that of the type-IV interaction. The exception to this is for the larger values of θ_s, when $n = 1.1$ and 1.2.

It is also noticed from Fig. 8 that as n increases, thereby making the cowl geometry more elliptic, the angular region over which the type-IV interaction occurs is less. Furthermore, the peak pressure decreases and the location of the largest value of pressure moves downward along the cylinder surface.

Figures 9–11 show a comparison of the surface pressure for various shock impingement angles (SIAs) for each of the geometries. These figures highlight the trends shown in Fig. 8. Note also that some of the cases have separated regions for $\theta < 0$ deg.

Figure 12 shows a full view of the surface pressure distribution for various geometries with $\theta_s \approx 181$ deg and Fig. 13 shows a close view of the peak pressure region. In these figures notice that the width of the jet decreases, as given by the angular extent of the surface pressure distribution, and the value of the peak pressure decreases as n increases. As indicated in Fig. 8, Figs. 12 and 13 show how the interaction moves down

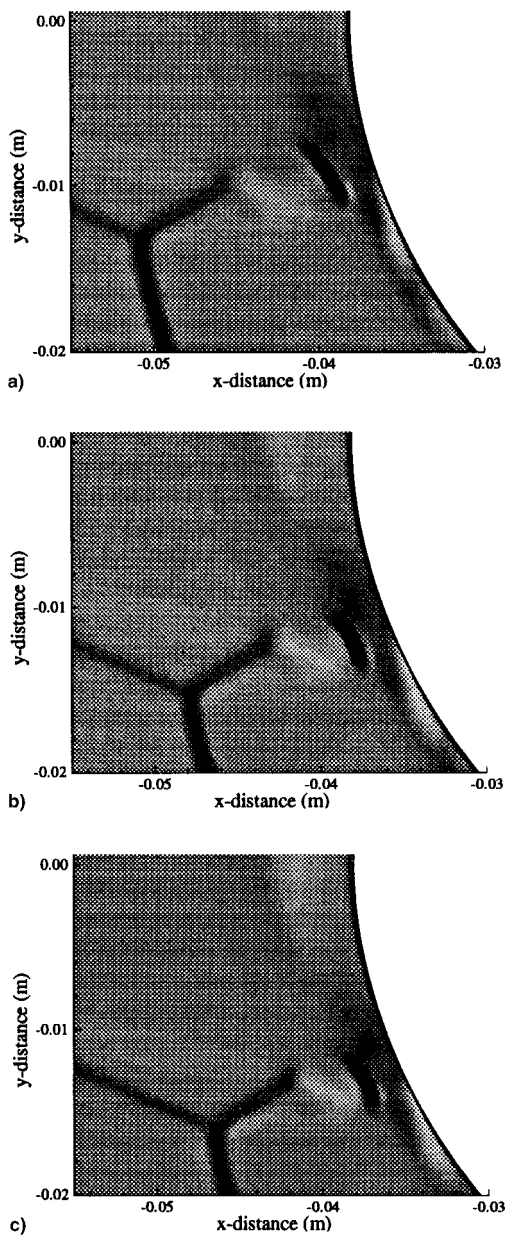

Fig. 21 Computational schlieren of the terminating shock associated with the supersonic jet for various shock impingement locations and $y = y_c^{1.05}$. θ_s = a) 176.5, b) 181.3, and c) 183.5 deg.

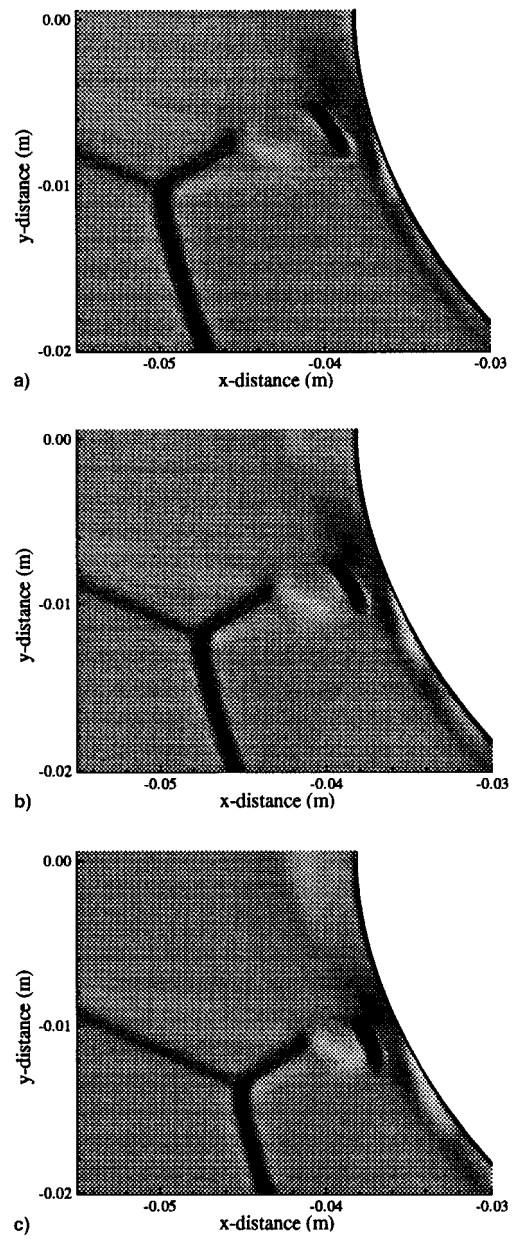

Fig. 22 Computational schlieren of the terminating shock associated with the supersonic jet for various shock impingment locations and $y = y_c^{1.1}$. θ_s = a) 175.1, b) 178.8, and c) 182.6 deg.

across the cowl surface as n increases for a constant value of θ_s.

Jet Unsteadiness

The time variation of the surface pressure for the $n = 1.1$ geometry with $\theta_s = 178.8$ deg is shown in Figs. 14 and 15. Notice from these figures that in addition to the jet motion there is an unsteady separation region. This separated region was noticed for all geometries when θ_s was approximately greater than 180 deg, the type-IV$^+$ region, described by Lind.[7]

The time history of the peak pressure for various θ_s are shown in Figs. 16–18. These figures are for $n = 1.05$, 1.1, and 1.2, respectively. In addition to the trends noted earlier, these figures show which of the interactions remain unsteady and which reach a steady-state solution. In addition, these figures show that as the body surface is made more elliptic in shape (n increasing) the interaction develops faster.

Another measure of the unsteadiness of the interaction can be made by looking at the L_2 norm of the density residual, as shown in Figs. 19 and 20. These plots show global unsteadiness, as opposed to Figs. 16–18, which show the localized unsteadiness associated with the supersonic jet. The low oscillation frequencies measured from Figs. 19 and 20 range from 2.7 to 12.6 kHz. These oscillations occurred when the jet impingement angles (JIAs), θ_s were greater than 180 deg.

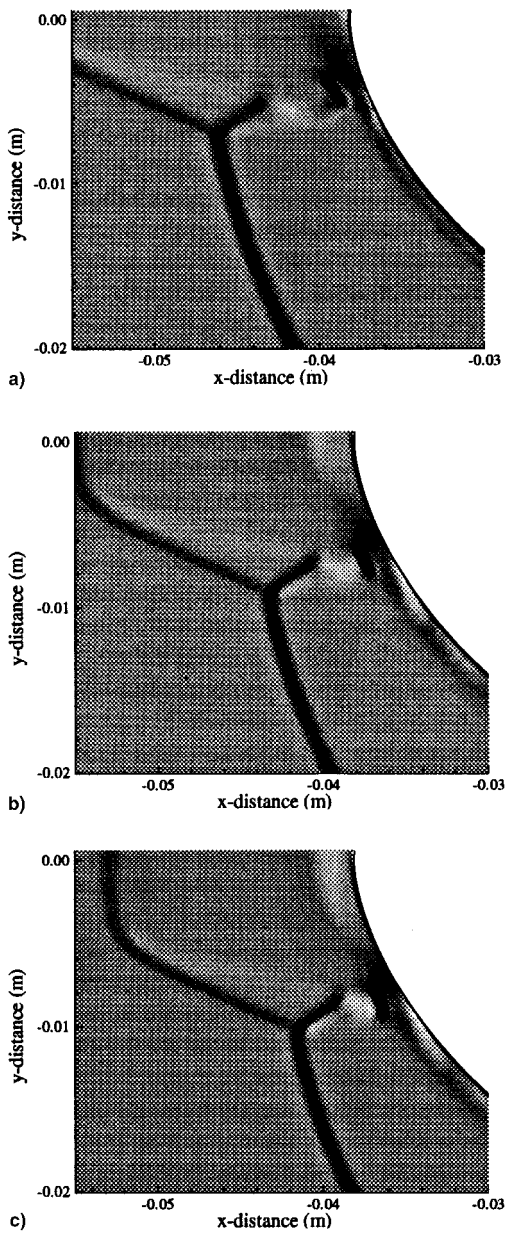

Fig. 23 Computational schlieren of the terminating shock associated with the supersonic jet for various shock impingement locations and $y = y_c^{1.2}$. θ_s = a) 176.9, b) 181, and c) 183.7 deg.

Detailed Flowfield Analysis

It was determined that for the configurations in which the interaction was unsteady, the terminating shock associated with the supersonic jet was either parallel with the body surface or angled downward. Computational schlierens of the shock configurations for some of the cases are illustrated in Figs. 21–23 and should be compared with the cases described earlier. These figures also show that as the cowl becomes more elliptic in shape the supersonic jet becomes more narrow and the interaction moves in closer to the cowl and becomes more compact.

Conclusions

The unsteady characteristics of the type-IV shock interaction for several different geometries have, for the first time, been numerically investigated using the thin-layer formulation of the Navier–Stokes equations coupled with a high-resolution, time-accurate, implicit TVD scheme.

The quasisteady state unsteadiness associated with interactions resulted from an unsteady separation region located above the jet impingement location. There is also a relationship between the orientation of the terminating shock associated with the supersonic jet and the measured unsteadiness. When the terminating shock is oriented such that it is either parallel with the body surface or makes an angle such that the flow through the shock is deflected downward, the interaction was found to be unsteady.

Changing the cowl geometry from a circular shape to a more elliptic shape tends to decrease the value of the peak pressure, move the location of the maximum peak pressure downward, decrease the width of the supersonic jet, and decrease the development time of the interaction.

Acknowledgments

This work was supported by the Office of Naval Research under the ONR postdoctoral program. The author would like to thank Helen Yee at the NASA Ames Research Center for the use of her TIMETVD code, Mark Lewis for his assistance, and Arinder Judge–Lind for reviewing the original manuscript. Appreciation is also expressed to the Jet Propulsion Laboratory Supercomputing Center for their generous computing time, the CADIG staff at the U.S. Naval Academy, and Jay Boris at the Naval Research Laboratory, who has graciously given me the time to complete this work.

References

[1]Bowcutt, K. G., "Optimization of Hypersonic Waveriders Derived from Cone Flows—Including Viscous Effects," Ph.D. Dissertation, Univ. of Maryland, College Park, MD, 1986.

[2]Edney, B., "Anomalous Heat Transfer and Pressure Distributions on Blunt Bodies at Hypersonic Speeds in the Presence of an Impinging Shock," Aeronautical Research Inst., Federal Aviation Administration, Rept. 115, Sweden, 1968.

[3]Holden, M. S., Wieting, A. R., Moselle, J. R., and Glass, C., "Studies of Aerothermal Loads Generated in Regions of Shock/Shock Interaction in Hypersonic Flow," AIAA Paper 88-0477, Jan. 1988.

[4]Prabhu, R. K., Stewart, J. R., and Thareja, R. R., "Shock Interference Studies on a Circular Cylinder at Mach 16," AIAA Paper 90-0606, Jan. 1990.

[5]Klopfer, G. H., and Yee, H. C., "Viscous Hypersonic Shock-on-Shock Interaction on Blunt Cowl Lips," AIAA Paper 88-0233, Jan. 1988.

[6]Gaitonde, D., and Shang, J. S., "On the Structure of an Unsteady Type IV Interaction at Mach 8," *Computers and Fluids Journal*, Vol. 24, No. 4, 1995, pp. 469–485.

[7]Lind, C. A., "A Computational Analysis of the Unsteady Phenom-

ena Associated with a Hypersonic Type IV Shock Interaction," Ph.D. Dissertation, Dept. of Aerospace Engineering, Univ. of Maryland, College Park, MD, 1994.

[8]Lind, C. A., and Lewis, M. J., "Unsteady Effects of a Hypersonic Type IV Shock Interaction," AIAA Paper 94-2945, June 1994.

[9]Keyes, J. W., and Hains, F. D., "Analytical and Experimental Studies of Shock Interference Heating in Hypersonic Flow," NASA TN D-7139, May 1973.

[10]Nowak, R., Holden, M. S., and Wieting, A. R., "Shock/Shock Interference on a Transpiration Cooled Hemispherical Model," AIAA Paper 90-1643, June 1990.

[11]Yee, H. C., and Harten, A., "Implicit TVD Schemes for Hyperbolic Conservation Laws in Curvilinear Coordinates," *AIAA Journal*, Vol. 25, No. 2, 1987, pp. 266–274.

[12]Pulliam, T. H., "Euler and Thin Layer Navier-Stokes Codes: ARC2D, ARC3D," *Notes for Computational Fluid Dynamics User's Workshop*, Univ. of Tennessee Space Inst., E02-4005-023-84, Nashville, TN, March 1984.

[13]Montagne, J. L., and Yee, H. C., "Comparative Study of High-Resolution Shock-Capturing Schemes for a Real Gas," NASA TM 100004, July 1987.

[14]Billig, F. S., "Shock-Wave Shapes Around Spherical- and Cylindrical-Nosed Bodies," *Journal of Spacecraft and Rockets*, Vol. 4, June 1967, pp. 822, 823.

[15]Hoffmann, K. A., *Computational Fluid Dynamics for Engineers*, Engineering Education System, Austin, TX, 1989.

[16]Sorenson, R. L., "A Computer Program to Generate Two-Dimensional Grids About Airfoils and Other Shapes by the Use of Poisson's Equation," NASA TM 81198, May 1980.

[17]Holden, M. S., Moselle, J. R., and Lee, J., "Studies of Aerothermal Loads Generated in Regions of Shock/Shock Interaction in Hypersonic Flow," NASA CR-181893, Oct. 1991.